CrossMark click for updates

Power coupling and utilization efficiencies of silicon-depositing plasmas in mixtures of H_2, SiH_4, Si_2H_6, and Si_3H_8

Mark A. Sobolewski[a)]
National Institute of Standards and Technology, 100 Bureau Drive, Gaithersburg, Maryland 20899

Robert G. Ridgeway, Mark D. Bitner, Dino Sinatore, and Patrick T. Hurley
Air Products and Chemicals, Inc., 7201 Hamilton Blvd., Allentown, Pennsylvania 18195

(Received 23 January 2014; accepted 9 June 2014; published 27 June 2014)

Adding Si_2H_6 or Si_3H_8 additives to SiH_4/H_2 discharges increases the growth rates for thin films of microcrystalline and amorphous silicon, but the reasons for this increase are not well understood. To better distinguish the chemical and physical from electrical effects of these additives, a comprehensive electrical study was performed for mixtures of H_2, SiH_4, Si_2H_6, and Si_3H_8. The power coupling efficiency, power utilization efficiency, voltage, current, impedance, and phase were measured as a function of total pressure, electrode gap, gas mixture, rf power, and time. The measurements identified a regime of pressure and gap in which the electrical behavior is optimized. In this regime, the power coupling efficiency is quite high and insensitive to gas mixture, and the power utilization efficiency also does not vary dramatically with mixture. Therefore, in this regime, chemical or physical effects of additives on growth rates predominate over electrical effects. Impedance models of the plasma and sheaths provide explanations for the optimized regime and its correlation with impedance phase. In addition, electrical signals were identified that can be used to detect a transient in the gas-phase density of silicon-containing molecules during deposition as well as other transient phenomena. The signals show promise for use in process monitoring and control.
© *2014 American Vacuum Society*. [http://dx.doi.org/10.1116/1.4885368]

I. INTRODUCTION

In recent years, thin-film silicon solar cell technology has seen great improvements.[1–8] The use of cells that have multiple absorbing layers, including microcrystalline silicon and hydrogenated amorphous silicon, has resulted in higher and more stable power conversion efficiencies.[1–4] The cost of producing such cells, however, is still higher than other thin-film solar technologies.[4] To become more commercially competitive, production costs must be reduced. One area for potential cost savings is the growth of microcrystalline silicon films.[1,3,4,8] Such films are usually produced by plasma enhanced chemical vapor deposition, which requires costly capital equipment. Also, they tend to have greater thicknesses and slower growth rates than other layers. If growth rates can be accelerated—while maintaining film quality—one could obtain major savings in production costs.

One way to increase growth rates is to mix additives such as disilane (Si_2H_6) or trisilane (Si_3H_8) into the silane/hydrogen (SiH_4/H_2) plasmas that deposit the films. Only relatively small and economical quantities of disilane are needed to significantly increase growth rates.[8] The cause of the faster growth rates is not well understood; several different causes are possible. The additives may participate in chemical reactions that form the precursor molecules that are necessary for film growth. Alternatively, by interacting with plasma electrons, the additives may alter the electron energy distribution function, thus affecting the formation of precursors from silane as well.[8] Finally, the additives may, via electrical effects, change the amount of power absorbed by plasma electrons, thus affecting the rates of precursor generation and film growth.

Such electrical effects are well known from previous studies of other electronegative or attaching gases, which, even when diluted, dramatically change the impedance, power coupling efficiency, and power utilization efficiency of discharges.[9] Power coupling efficiency is the fraction of applied power that is absorbed in the discharge rather than being dissipated in parasitic resistances in the surrounding circuitry. Power utilization efficiency is the fraction of discharge power that is absorbed by electrons in the plasma rather than ions in the sheaths. The electron power is considered useful power, since energetic electrons collide with gas molecules to produce reactive precursors necessary for film growth (as well as the ionization events needed to sustain the discharge). In contrast, when energetic ions collide with gas molecules or surfaces, their energy is mostly lost as heat. Ion bombardment may have harmful or beneficial effects on film properties, but in either case the power absorbed by ions is—from the point of view of generating precursor molecules—considered wasted power.

As a prerequisite to detailed investigations of the chemical and physical effects of the additives, we report here this comprehensive, quantitative study of their electrical effects. First, in Sec. II, we describe the experimental apparatus and methods, including the careful calibration and characterization procedures that are needed to assure accurate electrical measurements. Then, we present and explain measurements of power coupling efficiency versus pressure and electrode gap in Sec. III and versus gas mixture in Sec. IV. Section V reports measurements as a function of rf power, from which power utilization efficiencies are determined. Section VI presents electrical parameters that were observed to change

[a)]Electronic mail: mark.sobolewski@nist.gov

Redistribution subject to AVS license or copyright; see http://scitation.aip.org/termsconditions. Download to IP: 129.6.144.75 On: Fri, 27 Jun 2014 17:35:22

versus time during depositions and discusses the use of such measurements for process monitoring and control. A brief summary follows in Sec. VII.

II. EXPERIMENT

A. Cluster tool and deposition chamber

The deposition chamber used in these experiments, shown in Fig. 1, is part of a cluster tool that is equipped with robotics for handling silicon wafers of diameter 200 mm. Such wafers were used as substrates for all depositions. Usually the wafer surface was bare silicon, but in a few experiments designed to study deposition on glass, glass slides were mounted and bonded on top of the wafers. Wafers enter the chamber from the side and are placed on a grounded susceptor at the bottom of the chamber. The wafer and susceptor are heated from below by lamps. A motor raises and lowers the susceptor, thus varying the gap between the wafer and the powered electrode, which is directly above it.

The powered electrode is an anodized aluminum disk of diameter 300 mm, driven by a 13.56 MHz generator and matching network. Water coolant is supplied by plastic tubing so that the electrode remains electrically isolated from all plumbing. Inside the chamber the electrode is surrounded by a ring insulator several inches wide. This design seems preferable to the much narrower insulators used previously, which can induce plasmas in electronegative gases at high pressures to "collapse" into a ring-like discharge around the rim of the electrode.[9–11] The darkening in the center of the electrode gap[9,10] and the shift in the discharge impedance toward more capacitive phases at higher pressures[9] that accompany such collapses were not observed here. The powered electrode also serves as a showerhead through which gas flows into the chamber. Gas is pumped out through a port on the side of the chamber via a pressure control valve.

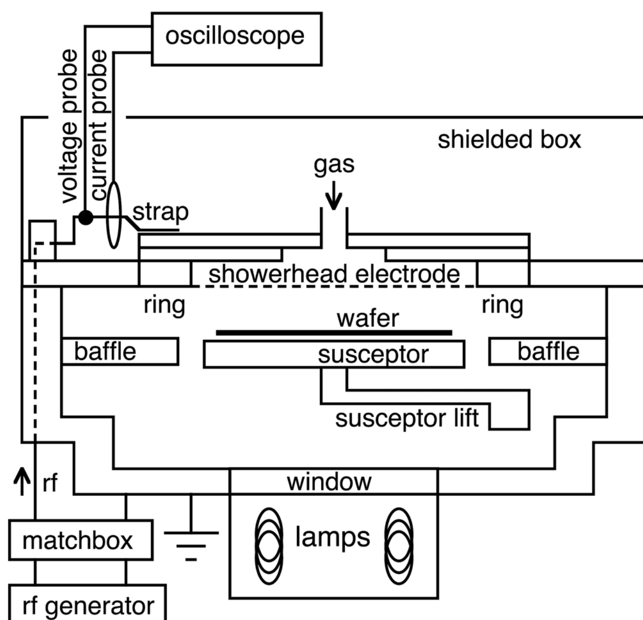

Fig. 1. Diagram of deposition chamber showing location of electrical probes.

The deposition chamber itself consists of two blocks of aluminum. One block forms the body of the chamber; the other is a top piece that supports the showerhead. The two pieces are connected with O-ring seals to maintain vacuum and hinges that allow the chamber to be easily opened for maintenance. The interior surfaces of the blocks, i.e., the chamber walls, are anodized. Insulating baffle structures located inward from the walls partially confine the plasma and separate it from some wall surfaces, but nevertheless allow gas to flow out the pumping port and allow optical access to the plasma, via a viewport and an optical fiber (not shown), which is connected to a spectrometer.

B. Current and voltage probes

From the matching network, which is mounted below the chamber, rf power is fed to a vertical post, which passes through cavities in the body and top pieces into a shielded box above the top piece. Normally, a short metal strap connects the post to a large plate that powers the showerhead. Here, the usual strap was replaced by a new one, modified to accommodate a Bergoz CT-D1.0-B current probe and a LeCroy PPE 6 kV voltage probe.[12] A flexible piece of silicone foam was used to insulate the case of the current probe from the strap. The foam also helps to keep the current probe in a fixed position and orientation. The probes were connected to a digital oscilloscope via wires fed out through small holes drilled in the shielded box.

Probe signals digitized by the oscilloscope were transferred to a computer for analysis. Using a curve-fitting algorithm, we extracted the magnitude and phase of each significant Fourier component, including the components of voltage and current at the fundamental or driving frequency (13.56 MHz); voltage and current harmonics up to the fifth, at 54.24 MHz; and the dc component of voltage, i.e., the dc self-bias voltage. This article concentrates on the fundamental components. The harmonics are not discussed, since they contributed negligible power. Some comments on the dc self-bias are made in Sec. VI.

The attenuation of the voltage probe was calibrated against known, standard attenuators connected to the input of a second oscilloscope. The output voltage per amp of the Bergoz current probe was checked against a Pearson 2877 current probe,[12] which was used in previous work but has too low a maximum current for this study. Better agreement was obtained when the Bergoz probe cable was terminated at the oscilloscope with 50 Ω rather than 1 MΩ. Thus, all currents reported here were measured with 50 Ω termination. The timing or phase difference between the voltage and current signals was calibrated using the stray impedance of the electrode as a load of known phase, as it has a nearly pure capacitive impedance over a wide range of frequency. After calibration, the residual, systematic uncertainty at 13.56 MHz was ±1% in voltage, ±1% in current, and ±0.1° in phase.

C. Stray impedance

Although the current and voltage probes were mounted as close as possible to the discharge, they are nevertheless

Redistribution subject to AVS license or copyright; see http://scitation.aip.org/termsconditions. Download to IP: 129.6.144.75 On: Fri, 27 Jun 2014 17:35:22

separated from it by some distance. This separation introduces stray impedance, which can be represented by the simple circuit model shown in Fig. 2. The port on the left side corresponds to the location of the probes; the port on the right represents the plasma-exposed, bottom surface of the showerhead electrode. The inductance L and resistance R represent the strap on which the probes are mounted. The insulators that isolate the electrode from ground contribute the capacitance C. The conductance G represents all conduction paths to ground that are in parallel with C, for example, conductance through the coolant water. Because of L, R, C, and G, the current and voltage measured by the probes, denoted I_m and V_m, differ from the current and voltage delivered at the electrode surface, I_d and V_d. To determine I_d and V_d, one must first determine L, R, C, and G.

To determine G, the strap on which the probes were mounted was disconnected from the matching network and connected to a dc ohm-meter. The measured dc resistance, which can be taken to be $1/G$, was 0.4 MΩ, much larger than all relevant impedances at radio frequencies. Thus, we can ignore G here.

To determine C, L, and R, the dc ohm-meter was replaced by a variable-frequency signal generator and rf amplifier, which applied a low-voltage ($\leq$40 V) sinusoidal signal at frequencies ranging from 0.1 to 100 MHz. At each frequency f, the current and voltage were measured by the probes and the impedance $Z_o = V_m/I_m$ was calculated (where V_m and I_m are complex Fourier amplitudes, Z_o is also complex, and its subscript indicates open circuit, i.e., no load connected to the right-hand port in Fig. 2). The measurements were made with the hinged top of the chamber opened, to prevent the capacitance of the electrode gap[13] or other fringing capacitances from acting as a load.

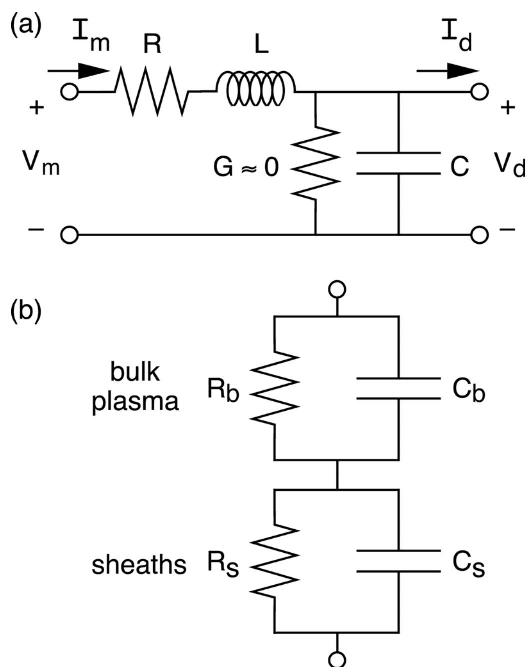

FIG. 2. (a) Circuit model of the stray impedance between the probes (the port on the left) and discharge (the port on the right) including series resistance R, series inductance L, parallel conductance G, and parallel capacitance C. (b) Circuit model of the discharge itself comprising the resistance R_b and capacitance C_b of the bulk plasma in series with the resistance R_s and capacitance C_s of the sheaths.

The measured magnitude of Z_o is plotted versus frequency in Fig. 3. For most of the frequency range, we observed nearly ideal capacitive behavior, i.e., $|Z_o| = (2\pi fC)^{-1}$. Fitting this equation to the $|Z_o|$ data from 0.1 to 50 MHz, we obtain the straight-line fit shown in the figure and a value for $C = 125$ pF. Above 50 MHz, $|Z_o|$ diverges from the fit and undergoes a sharp minimum that is produced by the series resonance of C and L. The observed frequency of the resonance, $f_r = 93.5$ MHz, together with the circuit model prediction $2\pi f_r = \omega_r = (LC)^{-1/2}$, yields a value for $L = 23$ nH.

Estimates for R were obtained at $f \approx f_r$, where $|Z_o| \approx R$, according to the circuit model. Obtaining R from $|Z_o(f_r)|$ can be problematical, however, when f_r is so high. First, statistical and systematic uncertainties are larger at high frequencies, and therefore, $|Z_o(f_r)|$ covered a rather broad range, 0.52 Ω–0.97 Ω. Second and more importantly, resistances at radio frequencies have a frequency dependence due to the skin effect. Thus, $|Z_o(f_r)|$ may be a poor estimate of R at $f \ll f_r$. Consequently, we scaled the measured values of $|Z_o(f_r)|$ with the $f^{1/2}$ scaling expected for good conductors to obtain R at our frequency of interest, 13.56 MHz. The resulting scaled values were $0.20\ \Omega \leq R \leq 0.37\ \Omega$.

Alternative methods for characterizing stray impedance, such as unterminating and de-embedding[14] or the open- and short-circuit method,[13] are more general than the approach used here, since they do not assume any particular circuit model. Such methods require additional measurements at conditions other than open circuit; one must perform measurements with known loads, a probe, or a short circuit

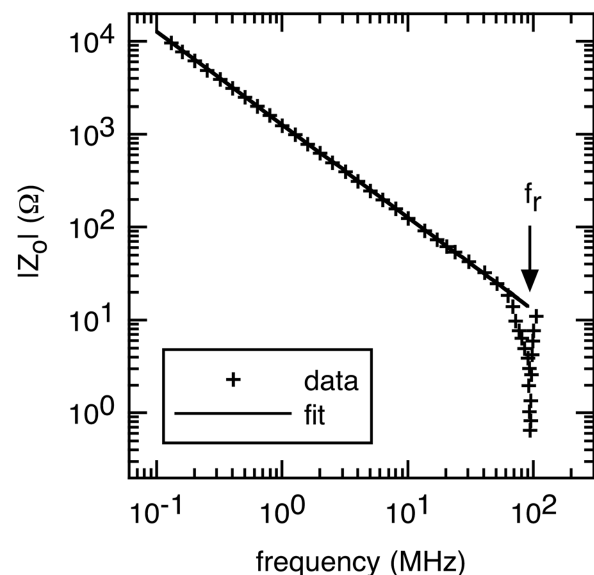

FIG. 3. Magnitude of the impedance |Zo| measured by the probes with the chamber open and electrode open-circuited (symbols) and a fit to the data for a model with a single constant capacitance (line). An arrow indicates the resonant frequency f_r.

Redistribution subject to AVS license or copyright; see http://scitation.aip.org/termsconditions. Download to IP: 129.6.144.75 On: Fri, 27 Jun 2014 17:35:22

connected to the right-hand port in Fig. 2. The ideality observed in Fig. 3, however, suggests that such additional measurements are not necessary. Furthermore, short-circuit measurements, in particular, would be difficult to achieve, since an effective short circuit must have an inductance $\ll L$, and L here is quite small. For example, using a sheet of metal foil to short-circuit the showerhead to the top wall of the chamber produced a "short circuit" that had an inductance of $\sim$20 nH, comparable to L. Similarly, short circuit measurements do not yield any precise information about R, because the resistance contributed by the short circuit is unknown. Nevertheless, measurements at short circuit (at 13.56 MHz) did provide a value of 0.3 Ω for the combined resistance of the short circuit plus R. This value can be used as an upper bound for R, thereby reducing our best estimate for R at 13.56 MHz, and its uncertainty, to $R = 0.25\ \Omega \pm 0.05\ \Omega$.

Short-circuit measurements can also be used to detect the impedance of insulating layers on electrode surfaces.[11] Here, such measurements indicated that the anodization layer on the showerhead electrode had a negligible ($\leq$0.1 Ω) impedance at 13.56 MHz. This result is explained by the thinness, high dielectric constant, and large area of the layer.

D. Discharge current, voltage, impedance, and power

Once the stray impedance has been characterized, the discharge current and voltage are obtained as follows. First, the complex Fourier components V_m and I_m measured during discharge operation are operated on to account for magnitude and phase calibration. Then, the calibrated V_m and I_m are inserted, along with C, L, and R, into the circuit equations

$$V_d = V_m - (R + i\omega L)I_m \tag{1}$$

and

$$I_d = -i\omega C V_m + (1 + i\omega RC - i\omega^2 LC)I_m, \tag{2}$$

to obtain I_d and V_d, the corresponding complex components of current and voltage at the surface of the rf-powered showerhead electrode. Here, $\omega = 2\pi f$, where f is the frequency of the components I_m, V_m, I_d, and V_d. From I_d and V_d, we obtain the impedance $Z_d = V_d/I_d$, its magnitude $|Z_d|$, its phase ϕ_d, and the delivered power

$$P_d = (1/2)|V_d||I_d|\cos\phi_d. \tag{3}$$

For comparison, we also calculate the total impedance seen by the probes, $Z_m = V_m/I_m$, its magnitude $|Z_m|$, its phase ϕ_m, and the power flowing past the probes

$$P_m = (1/2)|V_m||I_m|\cos\phi_m. \tag{4}$$

For our experimental conditions, Z_d is the sum of a largely resistive impedance contributed by the plasma in series with a largely capacitive impedance contributed by the sheaths. Therefore, it is useful to define two additional parameters: the equivalent series resistance

$$R_d = \mathrm{Re}(Z_d) = |Z_d|\cos\phi_d, \tag{5}$$

and the equivalent series reactance

$$X_d = \mathrm{Im}(Z_d) = |Z_d|\sin\phi_d, \tag{6}$$

where $Z_d = R_d + iX_d$.

Here I_d, V_d, $|Z_d|$, ϕ_d, P_d, R_d, and X_d are called the "discharge" or "delivered" parameters. They do not include the stray impedances in Fig. 2 and are therefore—compared to the measurements I_m, V_m, etc.—more representative of the discharge itself. Strictly speaking, however, they include everything on the discharge side of the circuit in Fig. 2. Thus, they (and the dc self-bias voltage) may contain small contributions from the wafer, the susceptor on which it is placed, the gap between them,[15] layers on chamber surfaces, and the return current path through the chamber.

The uncertainty of each parameter was obtained by propagating through Eqs. (1)–(6) the statistical uncertainty in measured $|V_m|$, $|I_m|$, and ϕ_m data as well as the systematic uncertainties in the magnitude and phase calibrations, C, L, and R. Statistical uncertainties were usually small. Systematic uncertainties were almost always dominant.

E. Deposition process

For each deposition, the same sequence of steps was performed. First, the wafer from the preceding run (if any) was removed, and the chamber was cleaned by an NF_3 plasma. The endpoint of the clean was monitored by the optical emission spectrometer. Next, a chamber "seasoning" step deposited a small amount of film on chamber surfaces, to give these surfaces a reproducible starting condition for the deposition and to immobilize any particulates that may have been liberated during the clean. After seasoning, a wafer was loaded into the chamber and a brief H_2 pretreatment was performed, followed by a deposition. The wafer temperature during deposition was always 220 °C. Following each deposition, the wafer was removed, and the cycle began again with another clean.

III. RESULTS VERSUS PRESSURE AND GAP

A. Power coupling efficiency

Before investigating the effects of varying gas mixtures and additives, we first characterized the effects of electrode gap and total pressure, for a single mixture of 25 SCCM SiH_4 and 250 SCCM H_2. The rf power applied at the generator, P_a, was held constant at 100 W, while the gap was varied from 4 to 23 mm and the pressure was varied from 133 to 667 Pa (1 to 5 Torr). Pressures higher than this range were not investigated, since they were known to produce dusty plasmas and low quality films.

Results are shown in Fig. 4. The power P_m measured at the probes, shown in Fig. 4(a), and the power P_d delivered to

Redistribution subject to AVS license or copyright; see http://scitation.aip.org/termsconditions. Download to IP: 129.6.144.75 On: Fri, 27 Jun 2014 17:35:22

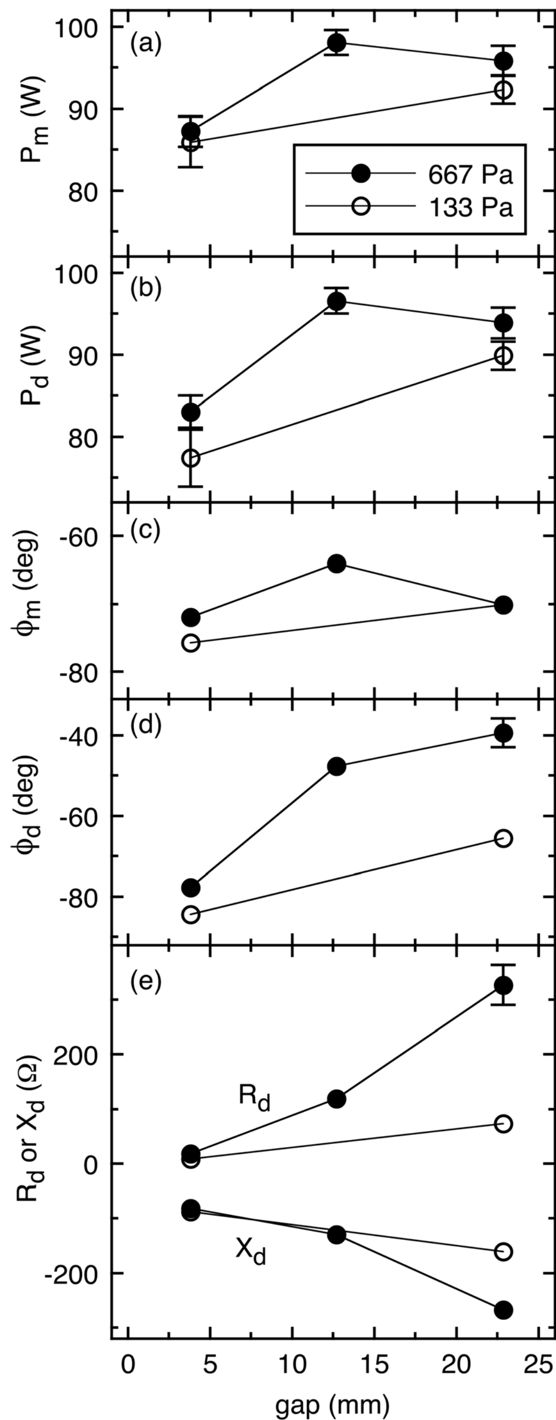

FIG. 4. Electrical parameters as a function of electrode gap and pressure, all at 25 SCCM SiH_4, 250 SCCM H_2, and generator power $P_a = 100$ W, including (a) the power P_m at the probes, (b) the power P_d delivered to the discharge, (c) the impedance phase ϕ_m at the probes, (d) the impedance phase ϕ_d of the discharge, and (e) the equivalent series resistance R_d and reactance X_d of the discharge. Uncertainties that are not shown are smaller than the symbol size.

the discharge, shown in Fig. 4(b), have qualitatively similar behaviors. Both P_m and P_d increase slightly with increasing pressure and tend to increase with increasing gap, except when going from 13 to 23 mm at 667 Pa (5 Torr). The difference P_a–P_m, where $P_a = 100$ W, represents power losses occurring between the generator and the probes (most likely in the matching network) whereas P_m–P_d is the power dissipated in the strap resistance R. Comparison of P_a–P_m with P_m–P_d shows that both types of losses have roughly similar behaviors. They also have roughly comparable magnitudes, although P_a–P_m is, throughout Fig. 4, always larger.

The best coupling obtained in Fig. 4 was at 667 Pa and 13 mm. Those conditions gave a coupling efficiency P_d/P_a, including uncertainty, of 0.95–0.98. Consequently, that pressure and gap were chosen for the subsequent measurements in Secs. IV–VI.

B. Impedance and phase

The changes in P_m and P_d in Figs. 4(a) and 4(b) are related to changes in the impedance phases ϕ_m and ϕ_d. The phase ϕ_m of the total load downstream of the probes, shown in Fig. 4(c), is strongly correlated with P_m in Fig. 4(a). The highest value of P_m is obtained at the most resistive, i.e., least negative, value of ϕ_m. Conditions that make ϕ_m more negative produce smaller P_m. The phase ϕ_d of the discharge impedance, shown in Fig. 4(d), displays behavior different from ϕ_m, but similar to previous experiments[9,16] that found peak power coupling efficiencies for ϕ_d at or near −45°. Here, in Fig. 4, the peak P_m and P_d both occur when $\phi_d = -47.6°$, the closest point to −45°. When ϕ_d shifts away from −45°, toward either more negative or less negative values, both P_m and P_d decrease.

The shifts in ϕ_d seen in Fig. 4(d) are explained by considering the equivalent series resistance and reactance, R_d and X_d from Eqs. (5) and (6), shown in Fig. 4(e). There, R_d increases and X_d becomes more negative at wider gaps or higher pressure. The changes in R_d and X_d act in opposite directions on the overall phase ϕ_d. The percentage changes in R_d are larger than in X_d, however, and therefore R_d dominates, making the overall phase ϕ_d shift away from −90° toward 0° as the pressure or gap increases.

The behavior of the delivered power P_d can be explained by the changes in R_d. At low pressures or narrow gaps, an increase in R_d causes more of the total voltage drop to occur across R_d rather than the strap resistance R (or other series resistances upstream of R) thus increasing P_d. When R_d becomes too large, however, further increases in R_d shunt more current through the parasitic parallel capacitance C (as indicated by the shift in measured phase ϕ_m toward more negative values when the gap is increased from 13 to 23 mm at 667 Pa). This shunting decreases the discharge current I_d, thereby decreasing the power P_d. Thus, there is an optimal value of R_d, and, in turn, an optimal value of the phase ϕ_d. The remainder of this section presents model equations necessary to provide quantitative explanations of the behavior in Fig. 4 (and other results in subsequent figures) as well as predictions for the value of the optimal phase.

C. Impedance of the plasma and sheaths

For our experimental conditions, the plasma contributes an impedance that is predominantly resistive. For a spatially uniform region of bulk plasma of length D and cross sectional area A, this ohmic resistance is given by

Redistribution subject to AVS license or copyright; see http://scitation.aip.org/termsconditions. Download to IP: 129.6.144.75 On: Fri, 27 Jun 2014 17:35:22

$$R_b = m_e \nu_e D / \left(n_e e^2 A\right), \quad (7)$$

where e, m_e, n_e, and ν_e are the charge, mass, number density, and collision frequency of electrons. The plasma also has an inductance due to electron inertia, but this can be neglected if $\omega \ll \nu_e$.[9] Values of ν_e for silane-hydrogen discharges obtained by Amanatides *et al.*[17] show that this criterion is easily satisfied. Here, ω/ν_e ranges from 0.017 at 133 Pa to 0.003 at 667 Pa. In addition, the plasma has a non-negligible bulk capacitive impedance

$$iX_b = -iY_b^{-1} = -i(\omega C_b)^{-1} = -iD/(\omega \varepsilon_0 A), \quad (8)$$

which arises from the flow of displacement current through the plasma. Because the ohmic current and displacement current flow in parallel, R_b and iX_b add in parallel, yielding a combined impedance

$$Z_b = R_b(1 - i R_b Y_b)/(1 + R_b{}^2 Y_b{}^2) \approx R_b - iR_b{}^2 Y_b. \quad (9)$$

Here, we have used the approximation $R_b{}^2 Y_b{}^2 \ll 1$, which can be shown to be valid using estimates for Y_b obtained by setting D in Eq. (8) equal to the electrode gap.

Additional impedance is contributed by the sheaths. In the high-frequency limit, where ω is much higher than the ion plasma frequency everywhere in the sheath, the displacement current dominates the electron and ion currents, such that the sheath impedance is nearly entirely capacitive. Using the Lieberman model for high-frequency, high-pressure, collisional sheaths,[18] the sheath impedance Z_s can be expressed as[19]

$$Z_s = iX_s = -0.803i\,(e\lambda_i/m_i)^{1/5}\, I_i^{-2/5}\,(V_{s1}/A\varepsilon_0)^{3/5}\omega^{-1}, \quad (10)$$

where λ_i is the ion mean-free-path, m_i is the ion mass, I_i is the ion current, V_{s1} is the fundamental amplitude of the sheath voltage, and ε_0 is the permittivity of vacuum.

The sheaths are in series with the plasma. Thus, the total discharge impedance is

$$Z_d = Z_b - 2iX_s \approx R_b - 2iX_s - iR_b{}^2 Y_b. \quad (11)$$

Here, we have assumed that the two sheaths are symmetric, i.e., each has impedance iX_s.

The behavior of R_d in Fig. 4(e) can now be explained using Eqs. (5), (7), and (11). Because of the factor D in Eq. (7), R_b and thus R_d are roughly proportional to the electrode gap. Departures from a direct proportionality, e.g., the positive curvature of the R_d versus gap plot at 667 Pa, arise because part of the gap is occupied by the sheaths, not the plasma. The increase in R_d with increasing pressure is explained by the factor ν_e in Eq. (7), although, apparently, part of this effect is canceled by an increase in n_e with pressure, as has been previously been noted by Amanatides *et al.*[17]

As for X_d, its behavior is explained by Eqs. (6)–(11). At narrow gaps or low pressures, the $-2iX_s$ term dominates the $-iR_b{}^2Y_b$ term in Eq. (11). For such conditions, X_d does not vary much with gap or pressure, because X_s in Eq. (10) has no dependence on D and only a weak $\lambda_i{}^{1/5}$ dependence on pressure. At wide gaps or high pressures, however, the $-iR_b{}^2Y_b$ term dominates, resulting in an X_d that, according to Eqs. (6)–(8) and (11), varies linearly with D and quadratically with pressure.

D. Optimal coupling criterion

Here, we obtain quantitative predictions for the value of phase ϕ_d that yields optimal power coupling. Specifically, we use the circuit in Fig. 2 to calculate the phase that minimizes losses in the strap resistance R. Essentially, the same circuit[20] and equations can also be used to consider losses in the matching network. In that case, R instead represents the series resistance at the output of the matching network, while C represents the total capacitance to ground of the showerhead and all other points in the circuit back to the matching network output.

We start with the discharge impedance Z_d from Eq. (11). In the narrow-gap or low-pressure limit, the $-i\,R_b{}^2Y_b$ term in Eq. (11) can be neglected, since it is dominated by the $-2iX_s$ term. Taking the parallel combination of Z_d and the parasitic capacitance C, one obtains a total impedance Z_c and an equivalent series resistance R_c given by

$$R_c + \mathrm{Re}(Z_c) = R_b/[(1 + C/C_S)^2 + \omega^2 R_b{}^2 C^2], \quad (12)$$

where $C_s = (-2\omega X_s)^{-1}$ is the combined capacitance of both sheaths. In terms of R_c, the discharge power P_d can be expressed as (1/2) $I_m{}^2 R_c$, whereas the power P_R lost in R is (1/2) $I_m{}^2 R$. Thus, $P_d/P_R = R_c/R$, and the power coupling (for constant R, C, and C_s) is maximized when $dR_c/dR_b = 0$, i.e., when

$$\tan\phi_d = -C/(C + C_S). \quad (13)$$

If $C \gg C_s$, this equation reduces to $\phi_d = -45°$, the value suggested by previous empirical studies.[9,16] If $C \approx C_s$, however, the optimal coupling occurs at $\phi_d > -45°$. On the other hand, if the analysis is repeated for wider gaps or higher pressures, by retaining the third term in Eq. (11), a more complicated result is obtained, which allows solutions at $\phi_d < -45°$, as well. Thus, the point of optimal coupling should not be expected to always exactly equal $-45°$, although one may expect it to be fairly close.

IV. RESULTS VERSUS GAS MIXTURE AND TOTAL FLOW

Measurements were performed for a wide range of gas mixtures. For some mixtures, electrical data showed a transient or time-dependent behavior, which is discussed in Sec. VI. First, however, we describe the steady-state results that were observed after any such transients had stabilized.

A. Power coupling efficiency

Figure 5 shows results for varying gas mixtures and total flows, all at a source power $P_a = 400$ W, a total pressure of

Redistribution subject to AVS license or copyright; see http://scitation.aip.org/termsconditions. Download to IP: 129.6.144.75 On: Fri, 27 Jun 2014 17:35:22

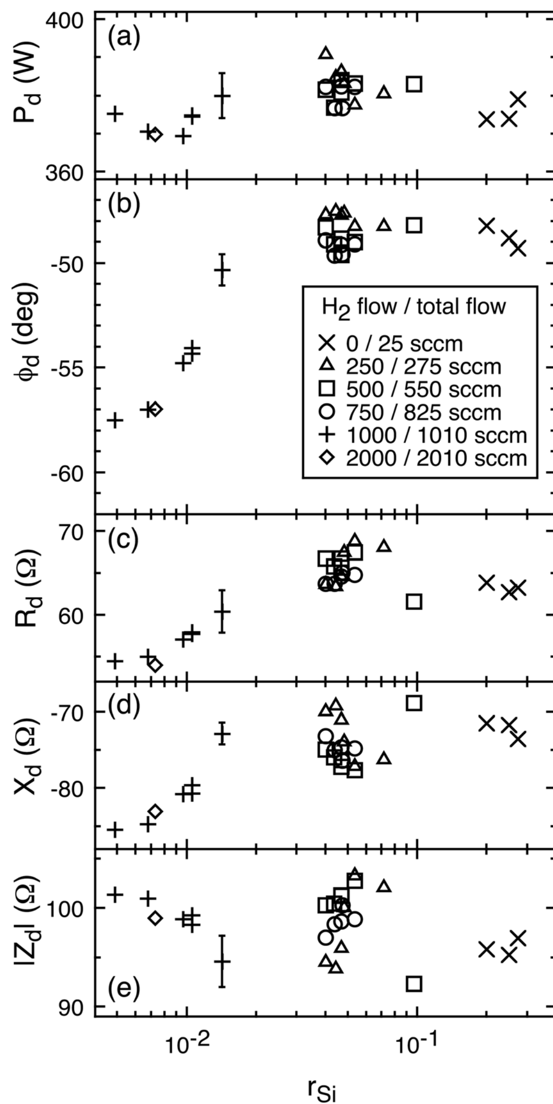

FIG. 5. Discharge electrical parameters for varying gas mixtures, all at 667 Pa, 13 mm gap, and applied power $P_a = 400$ W, plotted vs silicon atomic flow ratio r_{Si}. The legend gives the H_2 flow and total flow; within each series r_{Si} was varied by adjusting the flows of SiH_4, Si_2H_6, and Si_3H_8. The data are (a) power P_d, (b) phase ϕ_d, (c) equivalent series resistance R_d, (d) equivalent series reactance X_d, and (e) impedance magnitude $|Z_d|$. Uncertainties, which are dominated by systematic factors that affect all points nearly equally, are indicated by error bars on a single point per subfigure, at $r_{Si} = 0.014$.

667 Pa (5 Torr), and a gap of 13 mm. The data are plotted as a function of the silicon atomic flow ratio, r_{Si}, defined as the total flow of silicon atoms in all feed gases divided by the total flow of all atoms, Si and H. Measurements in pure SiH_4, Si_2H_6, and Si_3H_8 (at 25 SCCM) yield the three rightmost points, at $r_{Si} = 0.20$, 0.25, and 0.27, respectively. In addition, at $0.04 \leq r_{Si} \leq 0.1$, are data from each of the silicon-containing gases (and mixtures thereof) diluted 10:1 with H_2, at total flows of 275, 550, and 825 SCCM. Finally, at $r_{Si} \leq 0.02$, are data from the silicon-containing gases and mixtures diluted 100:1 (or for one point 200:1) at a total flow of 1010 (or 2010) SCCM. For clarity, the uncertainties—which are dominated by systematic factors that affect all points in each subfigure nearly equally—are indicated by error bars on a single point per subfigure, at $r_{Si} = 0.014$.

The power P_d delivered to the discharge, shown in Fig. 5(a), was quite high for all mixtures. All the data are within a few watts of 380 W, which gives a power coupling efficiency $P_d/P_a = 0.95$. Even including the uncertainties, all P_d data fall in the range $P_d > 360$ W, i.e., $P_d/P_a > 0.90$. The power P_m measured at the probes (not shown) was about 5–7 W higher than P_d but was otherwise quite similar.

In Fig. 5(a), there is little variation in P_d with r_{Si}, or with total flow at constant r_{Si}, or on substituting one silicon-containing gas for another at constant r_{Si} or constant total flow. Any differences in P_d with respect to these variables are on the order of 1%, comparable to the reproducibility of the measurements. If there is a dependence of P_d on the gas mixture or total flow it is too small to be detected within the reproducibility of the measurements.

B. Impedance and phase

Unlike the power P_d, the phase ϕ_d, shown in Fig. 5(b), does vary significantly with gas mixture. For $r_{Si} > 0.02$, $\phi_d \approx -48°$, but at $r_{Si} < 0.02$, ϕ_d shifts to more negative values, eventually reaching as low as $-57.5°$. But ϕ_d never reaches the ranges ($>-40°$ or $<-65°$) that were in Fig. 4 associated with a decline in power coupling efficiency. Apparently, the dependence of P_d on ϕ_d is not sharply peaked; rather it has a broad and flat maximum with very little change in P_d over a range of at least 10°.

Over the range of r_{Si} where ϕ_d becomes more negative in Fig. 5(b), R_d in Fig. 5(c) becomes smaller and X_d in Fig. 5(d) becomes more negative. These changes in R_d and X_d act in the same direction on ϕ_d; both contribute to making ϕ_d more negative. But they act in opposite directions on the impedance magnitude, $|Z_d|$, shown in Fig. 5(e), which thus remains relatively constant. This behavior differs from the results versus gap in Fig. 4, where increases in R_d coincide with X_d becoming more negative. Those results, as explained previously, arise from the plasma capacitance and the $-i\,R_b^2 Y_b$ term which it contributes to Eq. (11). Here, however, at $P_a = 400$ W, the sheath term, $-2iX_s$, dominates.

The decrease in R_d at low r_{Si} can be explained by a decrease in ν_e or an increase in n_e [see Eq. (7)] as mixtures become more rich in hydrogen, as will be discussed further in Sec. IV C. Also, hydrogen-rich mixtures should have a lower average ion mass m_i in Eq. (10), which would make X_d more negative. Any of these changes in ν_e, n_e, and m_i would alter the way the voltage is divided between the plasma and its sheaths, producing an increase in sheath voltage V_{s1}, which would act in Eq. (10) to make X_d even more negative. These changes also affect how the power P_d is utilized within the discharge, as will be discussed in Sec. V.

C. Explanation and discussion

The behavior of R_d for different mixtures—in particular, its decrease at low r_{Si} in Fig. 5(c)—is ultimately caused by differences in the cross sections of the collision processes through which plasma electrons interact with gas molecules. One possible contribution to changes in R_d is a change in the collision frequency, ν_e, which can be expressed as

Redistribution subject to AVS license or copyright; see http://scitation.aip.org/termsconditions. Download to IP: 129.6.144.75 On: Fri, 27 Jun 2014 17:35:22

$$\nu_e = \sum_m \int_0^\infty u_e(E) N_m \sigma_m(E) dE, \tag{14}$$

where u_e and E are the speed and energy of electrons, N_m and σ_m are the number density and momentum transfer cross section of the *m*th molecular species, and the sum is over all molecular species. The momentum transfer cross-section of H_2 has a peak value, denoted σ_0, of only 1.8×10^{-15} cm^2,[21,22] while SiH_4 peaks at $\sigma_1 = 3.0\times10^{-15}$ cm^2,[23,24] and Si_2H_6 peaks at $\sigma_2 = 6.3\times10^{-15}$ cm^2.[24,25] Thus, dilution of SiH_4 or Si_2H_6 with H_2 reduces scattering, producing a decrease in ν_e, and thus in R_b and R_d as well.

Of course, fragmentation of the feed gases occurs in the plasma, and scattering from the fragments must also be considered. Scattering from H and H_2 are roughly comparable, judging from measured differential and integral cross sections for elastic scattering, which, at electron kinetic energies $E_e < 2$ eV are higher for H than H_2, but at $E_e > 2$ eV are higher for H_2.[26,27] Calculated total elastic cross sections of SiH, SiH_2, and SiH_3 are slightly below SiH_4 and about half of Si_2H_6.[28] Taken together, these results suggest that ν_e (in $H_2/SiH_4/Si_2H_6$ mixtures) should roughly scale as $N_0\sigma_0 + N_1\sigma_1 + N_2\sigma_2$, where N_0, N_1, and N_2 are the total number density of all molecules containing zero, one, or two silicon atoms, respectively. When operating at constant total pressure, fragmentation produces a decrease in N_1 and N_2 and an increase in N_0, which should reduce ν_e relative to the pure, unfragmented feed gases and make the variation in ν_e with hydrogen dilution weaker than would be expected for unfragmented feed gases.

The electron density n_e may also vary with gas mixture, via the ionizing collisions that produce electrons or attachment processes which remove them. Total cross sections for ionization have peak values of 1.2×10^{-15} cm^2 for Si_2H_6;[29] 5×10^{-16} cm^2 for SiH_4,[29,30] SiD, SiD_2, and SiD_3;[31] and 1×10^{-16} cm^2 for H_2 (Refs. 21 and 22) and H.[32] Therefore, dilution of Si_2H_6 or SiH_4 with H_2 should tend to decrease the ionization rate and n_e. On the other hand, attachment would act in the opposite direction, since cross sections for dissociative attachment are $\approx10^{-18}$ cm^2 for silane[33] and disilane,[34] but $\leq 2\times10^{-20}$ cm^2 for H_2.[21,35] These values for feed gases in the ground state may not be so relevant, however, since attachment is believed to be dramatically enhanced for electronically[36] or vibrationally[37] excited molecules, radicals,[38,39] or "dust" particles.[40] It appears that ionization effects dominate attachment, since microwave measurements of n_e show a weak decrease when SiH_4 is diluted by H_2.[41] This weak decrease in n_e would act to increase R_b, but it is apparently dominated by the larger decrease in ν_e upon dilution discussed above. Ionization effects may also cause the ion current to decrease with H_2 dilution, which, according to Eqs. (10) and (11), would contribute to the change observed in X_d.

Cross-section data are not available for Si_3H_8. Nevertheless, one may estimate them by extrapolating from SiH_4 and Si_2H_6. Such extrapolations would suggest that ν_e and n_e—and thus R_b, R_d, and P_d—for mixtures containing Si_3H_8 would be similar to other mixtures having the same r_{Si}, as is observed in Fig. 5.

The gas mixture effects seen here are smaller than those observed previously[9] in NF_3/Ar discharges. There, a strong dependence of impedance and phase on NF_3/Ar ratio presumably results from the very high attachment cross section[42] of NF_3. Here, however, all relevant molecules are much less electronegative than NF_3. The size of gas mixture effects are further limited here for the reasons discussed above. First, the relevant cross sections of silicon-containing molecules and molecules containing only hydrogen are not so very different. Second, the effects of scattering and attachment act in a different direction from ionization, and therefore they partially cancel each other out. Third, even pure silicon-containing gases, once they have been dissociated in the plasma, are to some extent diluted by H or H_2. Fourth and finally, the possibility that gas mixture effects could be amplified by positive "feedback" from changes in power coupling was minimized here by choosing appropriate values of the electrode gap and total pressure.

The relative weakness of gas mixture effects seen here should not be interpreted, however, as suggesting that the choice of mixture or additive is unimportant. Gas mixture does affect the efficiency with which power is used in the discharge, as will be shown in Sec. V. It also has other important effects to be discussed there.

V. RESULTS VERSUS POWER

A. Power utilization efficiency: Analysis

So far the discussion has focused on power coupling efficiency, which only concerns power losses outside of the discharge. Here, we consider the mechanisms by which power is absorbed within the discharge itself, either by electrons in the plasma or by ions in the sheaths. As discussed in Sec. I, the power absorbed by electrons, P_e, is considered useful power; the power absorbed by ions, $P_i = P_d - P_e$, is considered wasted; and the power utilization efficiency is therefore given by P_e/P_d.

Analysis[9,43–47] shows that P_e and P_i can be distinguished by measurements made at varying rf powers. First, consider P_e. Here (except at the widest gap), one may neglect displacement current in the plasma and assume that only ohmic current flows there. Thus,

$$P_e = I_d{}^2 R_b. \tag{15}$$

Furthermore, because plasma electrons are produced by P_e, one may assume that their density n_e should vary in direct proportion to P_e when the source power is varied. This condition, plus Eq. (7) indicates that[43]

$$P_e = k_e I_d, \tag{16}$$

where the proportionality factor k_e is independent of power, current, voltage, and electron density (although it may vary with gas mixture or total pressure).

The ion power P_i can be derived from sheath models. At high frequencies, the ion current I_i does not vary over the rf cycle. Therefore, $P_i = I_i V_{s0}$, where V_{s0} is the dc sheath

Redistribution subject to AVS license or copyright; see http://scitation.aip.org/termsconditions. Download to IP: 129.6.144.75 On: Fri, 27 Jun 2014 17:35:22

voltage. Furthermore, at high frequencies, the sheath displacement current dominates I_i, and thus the sheath impedance is nearly entirely capacitive, such that $V_{s1} = iX_sI_d$, with X_s given by Eq. (10). Using the sheath model[18] from which Eq. (10) is derived to relate V_{s0} and V_{s1}, we obtain $P_i = k_iI_d^{5/2}$, where the factor k_i is independent of voltage, current, power, n_e, and I_i, but may vary weakly with pressure and gas. Thus,

$$P_d = P_e + P_i = k_eI_d + k_iI_d^{5/2}. \tag{17}$$

So far, we have assumed very asymmetric sheaths, such that all of P_i is contributed by one sheath, but Eq. (17) is equally valid if the sheaths are symmetric or if each sheath voltage is a constant fraction of their total voltage. The latter condition is roughly satisfied here, based on estimates of the sheath voltages obtained from the measured total voltage, dc self bias voltage, estimated plasma voltage $|V_d| \cos(\phi_d)$, and Ref. 48. These estimates also show that the sheath voltages are in the high-voltage range[19] over which Eq. (10) is valid.

Using Eq. (17), the current-dependence of P_d—or related parameters such as R_d from Eq. (5) or the resistive voltage $|V_d| \cos(\phi_d)$—can be fit by the sum of two power laws to determine P_e and P_i.[43–47] Alternatively, one can obtain P_e and P_i from the log–log slope, $\partial\ln(P_d)/\partial\ln(I_d)$.[9] That method, however, tends to give noisy results, since computing a slope or derivative amplifies noise. Thus, here, we instead used a curve-fitting method.

B. Power utilization efficiency: Results

In Fig. 6(a), measurements of the discharge current I_d are plotted as a function of discharge power P_d. Results were obtained for a variety of mixtures, but the only significant variation in I_d or P_d with gas mixture was that I_d was slightly higher for mixtures at low silicon atomic flow ratios, $r_{Si} < 0.02$, compared to mixtures at $r_{Si} > 0.02$. Therefore, results for all mixtures within each range were averaged, and, for clarity, only the average values are plotted in Fig. 6(a). Data were obtained and are shown at applied powers P_a of 100–800 W for $r_{Si} > 0.02$; and at 400–700 W for $r_{Si} < 0.02$. The total uncertainty in the data points (before averaging mixtures) as well as the variations with mixture within each range are comparable to the size of the symbols.

Also shown in Fig. 6(a) are two fits of Eq. (17) to the data, one for each range of r_{Si}. From the values of the fitting parameters, k_e and k_i, we determined the electron power P_e, the ion power P_i, the power utilization efficiency P_e/P_d, and the fraction of discharge power lost to ions P_i/P_d. These are all plotted in Figs. 6(b) and 6(c), for both ranges of r_{Si}. For either range of mixtures, P_e/P_d in Fig. 6(b) declines from near 95% at $P_d = 100$ W to slightly above 50% at $P_d = 800$ W. This decline indicates that power is being used less efficiently at higher powers. Nevertheless, as shown in Fig. 6(c), P_e itself continues to increase with increasing power and it still has an appreciable slope at $P_d = 800$ W. The slope suggests that it may be worthwhile to increase the power above 800 W, to further increase P_e and presumably the deposition rate as well. In practice, however, this potential benefit is outweighed by other, more important considerations such as the unwanted formation of "dust" particles, which has been observed at high applied powers.

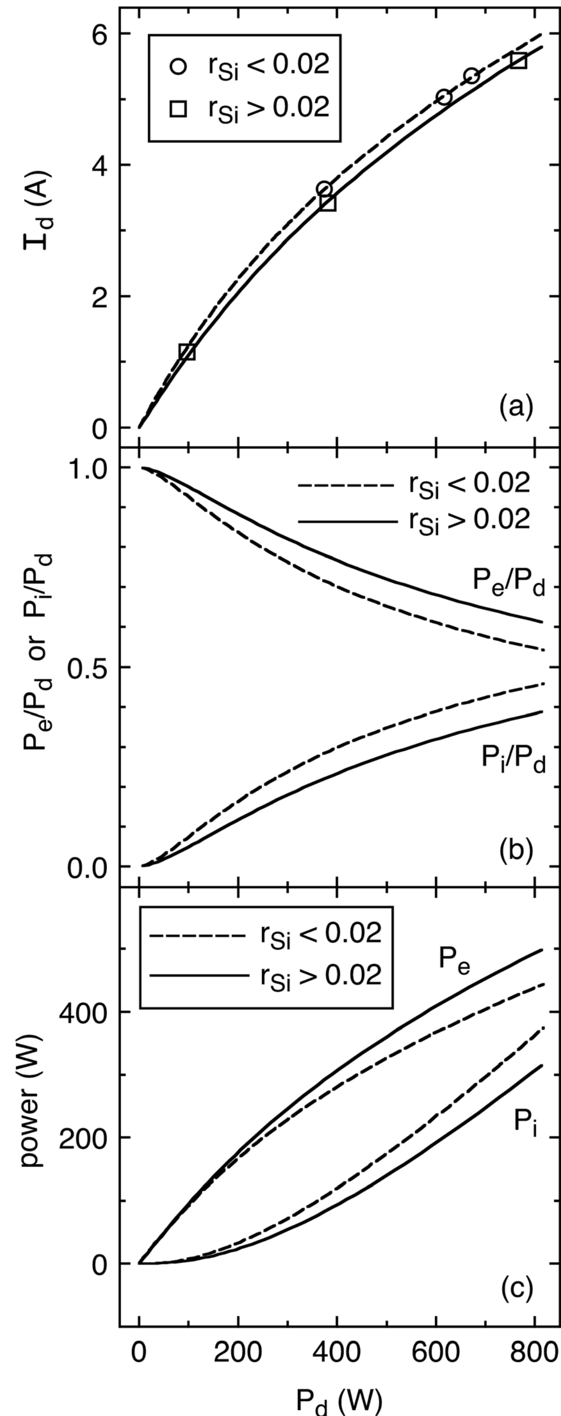

FIG. 6. (a) Measurements of discharge fundamental current I_d vs discharge power P_d, for mixtures with silicon atomic flow ratio $r_{Si} < 0.02$ (circles) and > 0.02 (squares), all at 667 Pa and 13 mm gap. Also shown are fits of the $r_{Si} < 0.02$ (dashed) and $r_{Si} > 0.02$ (solid) data by Eq. (17), and results obtained from the fits including (b) the power utilization efficiency P_e/P_d and fraction of power lost to ions P_i/P_d, and (c) the electron power P_e and ion power P_i. Uncertainties in the measurements are the same size as the symbols.

Redistribution subject to AVS license or copyright; see http://scitation.aip.org/termsconditions. Download to IP: 129.6.144.75 On: Fri, 27 Jun 2014 17:35:22

The differences between the two ranges of r_{Si} are rather small, less than 0.06 for P_e/P_d in Fig. 6(b) and less than 12% for P_e in Fig. 6(c). These differences are related to the mixture effects discussed in Sec. IV. The decrease in R_d (or increase in $-X_d$) for mixtures at low r_{Si}, seen previously in Fig. 5, must produce a decrease in P_e and an increase in P_i, if the total power P_d is to remain constant.

Considering P_e alone, only a 12% difference in growth rates is expected going from $r_{Si} < 0.02$ to $r_{Si} > 0.02$. The observation that the actual difference in growth rates is much larger can be attributed to chemical or electron energy effects. Differences in P_e and P_i within each range of r_{Si} were even smaller and are indeed insignificant. Thus, differences in growth rates within each range can be attributed entirely to nonelectrical effects.

The analysis given here has neglected a third mechanism for power absorption: the heating of electrons emitted from the wafer or electrode surfaces. Ion-induced electron emission is expected to be weak. Ion energies and thus ion-induced yields should be very low at the pressures used here, based on ion cross section data[49] or extrapolations from measurements[50,51] made at lower pressures. Photoemission of electrons may be more significant, however. Either emission process would result in power absorption with the same current-dependence as P_i.[52] Thus, it is possible that some of the power identified as P_i in Fig. 6 is in fact not wasted but represents a useful heating of emitted electrons. This possibility would tend to make power utilization efficiencies even higher—and the variation of useful power with mixtures even smaller—than seen in Fig. 6.

VI. RESULTS VERSUS TIME

A. Power and phase transients

One type of transient we observed was associated with imperfections in the control system of the rf generator and matching network. This type includes underdamped or overdamped responses in P_m and P_d when the rf power was turned on and, more rarely, oscillations in P_m and P_d during processing. These changes in P_m and P_d were mirrored (in the opposite direction) in R_d, $|X_d|$, and $|Z_d|$, but the phase ϕ_d was not much affected.

In contrast, a second and more interesting type of transient was most visible in ϕ_d. One example is shown in Fig. 7, for a mixture of 1000 SCCM H_2, 4 SCCM SiH_4, and 6 SCCM Si_3H_8 (such that $r_{Si} = 0.011$) at $P_a = 400$ W. Starting at time $t = 0$, when the rf power was turned on, slow changes were observed in all the parameters. The change in P_d in Fig. 7(a) was rather small, only 2%, while the change in ϕ_d in Fig. 7(b) was quite large, $-5°$. For R_d, X_d, and $|Z_d|$, shown in Figs. 7(c)–7(e), the changes—5%, 13%, and 6%, respectively—were all larger than the 2% change in P_d. The change in P_d is too small to account for the changes in ϕ_d, R_d, X_d, and $|Z_d|$, and for R_d it is in the wrong direction. A decrease in P_d should reduce the electron density in the plasma, causing R_d to increase, not decrease. Thus, the changes in Figs. 7(b)–7(e) cannot be attributed to fluctuations in power.

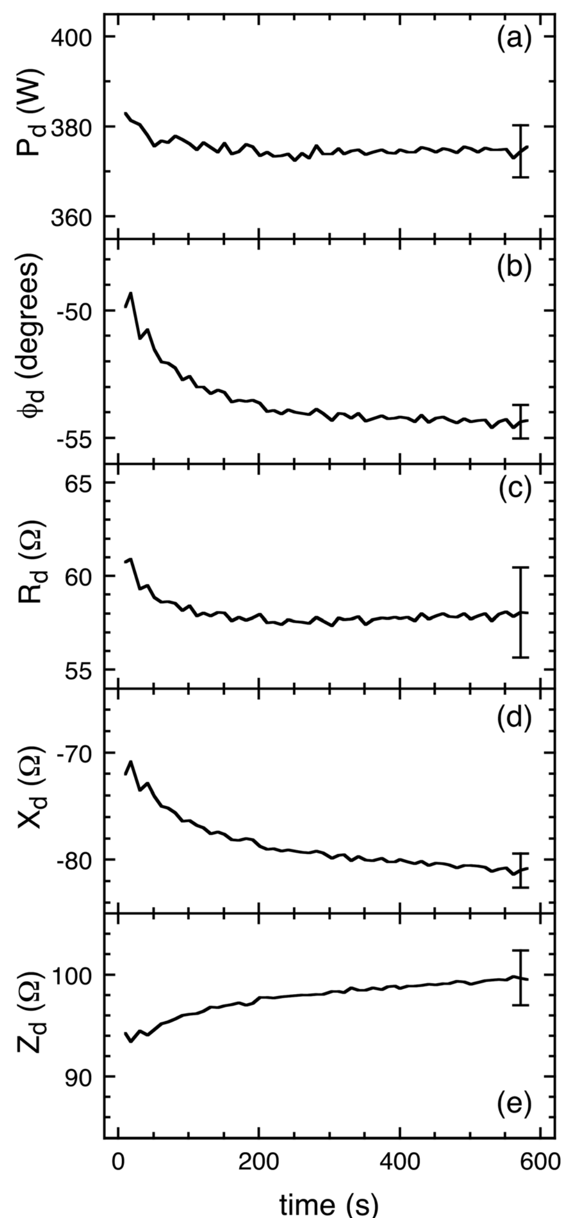

FIG. 7. Discharge electrical parameters vs time during deposition of a microcrystalline silicon film for 1000 SCCM H_2, 4 SCCM SiH_4, 6 SCCM Si_3H_8, $P_a = 400$ W, 667 Pa, and 13 mm gap. The data are (a) power P_d, (b) impedance phase ϕ_d, (c) equivalent series resistance R_d, (d) equivalent series reactance X_d, and (e) impedance magnitude $|Z_d|$. Uncertainties, which are dominated by systematic factors that affect all points nearly equally, are indicated by error bars on a single point of each curve.

Transients similar to those seen in Fig. 7 were observed for all highly diluted mixtures having a silicon atomic flow ratio $r_{Si} < 0.02$. All showed transients in the same directions and with the same time-dependence as Fig. 7, although their magnitudes were not always the same. For silicon-rich mixtures having $r_{Si} > 0.02$, however, no such transients were observed.

Exponential fits of the transients in Fig. 7 give time constants of about 100 s. Such a slow time scale may at first suggest the hypothesis that the transients are related to a change occurring on the wafer, electrode, or chamber surfaces, which influences the plasma via electron emission. Closer

Redistribution subject to AVS license or copyright; see http://scitation.aip.org/termsconditions. Download to IP: 129.6.144.75 On: Fri, 27 Jun 2014 17:35:22

examination shows this emission hypothesis is unlikely. The yield of ion-induced emission is expected to be small for reasons already discussed, whereas photoemission would produce behavior opposite to that observed. Because amorphous and monocrystalline silicon have different bandgaps, one might expect a change in photoemission yield at high r_{Si} as the amorphous film begins to cover the crystalline substrate. In contrast, microcrystalline and monocrystalline silicon have similar bandgaps, and therefore little change in photoemission would be expected at values of r_{Si} low enough to produce microcrystalline films. Furthermore, the same transients were observed even when glass slides were mounted on top of the silicon substrates.

A better explanation for the transients is a decay in the gas-phase density of silicon-containing molecules, as has been observed previously by optical emission,[5–7] infrared absorption,[53] and mass spectrometry.[54] This explanation is consistent with the data in Fig. 7, as can be seen by comparing with the (steady-state) mixture-dependences in Fig. 5. When r_{Si} approaches the steady state value of 0.011 from above in Fig. 5, all the changes seen in Fig. 7 are reproduced. The absence of transients for mixtures at $r_{Si} > 0.02$ can also be explained. For such mixtures, the gas-phase density of silicon-containing molecules may still be varying, but, according to the data in Fig. 5, the electrical parameters are not sensitive to changes in r_{Si} for $r_{Si} > 0.02$.

To account for their optical emission transients, which show SiH emission intensity falling with time both absolutely and with respect to H emission, Van den Donker *et al.*[5] propose two mechanisms. The first is a "transient depletion" or diffusion process, which occurs on a time scale $\leq$100 s. In this mechanism, which has been thoroughly studied and modeled, silicon-containing feed gas that is initially present in regions where no plasma is ignited takes time to diffuse into the volume occupied by plasma and be dissociated there. The plasma is therefore initially rich in silicon feed gases. As diffusion proceeds the silicon content in the plasma falls until finally the diffusion process is completed and a steady-state silicon content is established. To account for decreases in SiH emission intensity observed on longer time scales, 10^2–10^4 s, Van den Donker *et al.* propose a second mechanism, "long-term drift," which is not well understood but may be related to a gradual heating of the chamber wall by the plasma.[5] Presumably, surface reactions that remove silicon from (or release hydrogen to) the gas phase proceed faster as the walls gradually become hotter.

To test these and other possible mechanisms, additional experiments were performed, as shown in Fig. 8. First, a normal deposition process was run, for a mixture of 1400 SCCM H_2, 18 SCCM SiH_4, and 2 SCCM Si_2H_6 at ~600 W. The transient in ϕ_d for this normal process is shown in Fig. 8(a). Then, in Fig. 8(b), the process was repeated, but at 150 s, the rf power was turned off for 60 s. If the transient were caused by some problem with the flow control system one would expect it to continue even when the plasma was off. In other words, ϕ_d at 210 s would be more negative than ϕ_d at 150 s, but this is not observed. If the transient were solely dependent on the thickness of the film deposited on

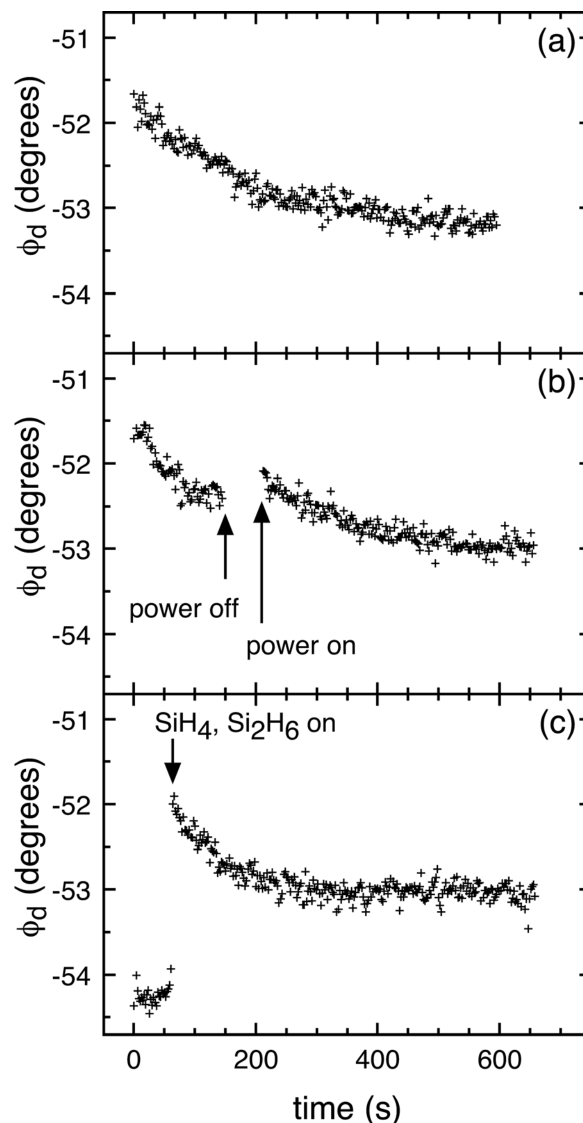

FIG. 8. Phase of discharge impedance vs time during deposition of microcrystalline silicon films for 1400 SCCM H_2, 18 SCCM SiH_4, and 2 SCCM Si_2H_6, $P_a \approx 600$ W, 667 Pa, and 13 mm gap. (a) Normal deposition process, (b) process with rf power interrupted for 60 s, (c) process with delayed introduction of silicon-containing gases. Uncertainties are $\pm 0.5°$.

the wafer or chamber surface, one would expect ϕ_d to be the same at 210 and 150 s, but this, too, is not observed. Instead, ϕ_d at 210 s is less negative than 150 s, i.e., the transient reverses itself when power is off and the plasma extinguished. This observation is consistent with either the "transient depletion" or "long-term drift" mechanism, with the reversal being caused either by the inflow of fresh, unreacted feed gas or the cooling of the chamber wall, respectively.

In Fig. 8(c), the plasma was ignited with only H_2 flowing, until, at time 60 s, the SiH_4 and Si_2H_6 flows were started. Otherwise, the conditions were the same as in Fig. 8(a). No transient was observed when only H_2 was flowing. As soon as the other gases were introduced, however, the transient began as usual and followed its usual course. This behavior cannot be explained by the "transient depletion" mechanism. Delaying the onset of silicon-containing feed gas should prevent the "transient depletion" phenomena, as shown by van

Redistribution subject to AVS license or copyright; see http://scitation.aip.org/termsconditions. Download to IP: 129.6.144.75 On: Fri, 27 Jun 2014 17:35:22

den Donker *et al.*[6] In contrast, transients related to heating of the chamber walls would perhaps not be too much affected by running 60 s of H_2 plasma. Thus the best explanation for our results is a "long-term drift" mechanism.

B. Process monitoring

Measurement of the transients discussed above would be useful not only in research studies but also in process development and manufacturing. Monitoring the delivered power P_d provides a means of detecting faults in the rf generator or matching network that might otherwise go unnoticed. Transients in the gas-phase density of silicon-containing molecules are also important, as they degrade the quality of the films being grown.[7] Perhaps it is possible to eliminate such transients, by appropriate design of chambers[7] or processes.[6] The measurements of phase and other electrical parameters presented here (either in addition to or as a substitute for optical emission) provide a useful means of monitoring how successful such design efforts are.

Additional information can be obtained by monitoring the dc self-bias voltage V_0, which is related to the spatial characteristics of the discharge. The sign of V_0 indicates which electrode—powered or grounded—has the larger effective area. For example, at low pressure (133 Pa) $V_0 < 0$, indicating that the plasma has expanded radially outward and come into electrical contact with a large area of the grounded chamber walls. At 667 Pa, however, the plasma contracts toward the radial center and no longer contacts a large area of wall. The wafer still acts as a grounded electrode, but its area is smaller than the rf-powered showerhead electrode, and therefore the opposite sign, $V_0 > 0$, is observed. In addition to pressure, changes in the extent of plasma expansion or contraction with gas mixture or time have also been detected by monitoring V_0. Such monitoring may provide useful information about the radial uniformity of the plasma and of the deposited film.

The dc bias may also provide a means of detecting "dust" particles. Some conditions at high rf power produce large amounts of particles, which eventually are incorporated in the growing film, giving it a cloudy appearance. We found that the cloudiness of films was correlated with the amplitude of noise in the dc bias, but additional experiments are needed to further verify and explain this correlation.

VII. CONCLUSIONS

The power coupling efficiency of the silicon-depositing plasmas studied here depends on the ohmic resistance of the bulk plasma. If the plasma resistance is very low, either because the pressure is too low or the electrode gap too narrow, an excessive voltage drop and power loss occurs in parasitic series resistances. In such cases, power coupling is improved by increasing the pressure or gap. If the pressure becomes too high or the gap too wide, however, an overly high plasma resistance causes current to be shunted across parasitic parallel capacitances rather than passing through the plasma, thereby increasing the power losses. Thus, there is an optimal value of the plasma resistance, which coincides with the impedance phase of the discharge being close to, but not necessarily exactly equal to, $-45°$. At and near this optimal condition, the power coupling efficiency is high, ≈ 0.95, and insensitive to variations in gas additives and mixtures or to other perturbations.

Variations in gas mixture do nevertheless affect the impedance of the discharge and its power utilization efficiency. When silicon-containing feed gases are sufficiently diluted by hydrogen to cause the silicon atomic flow ratio to fall below 0.02, the plasma resistance falls and the sheath capacitive impedance increases in magnitude. The fall in resistance is explained by decreased scattering and decreased attachment, but is partially compensated by decreased ionization. The increase in capacitive impedance is explained by a reduction in the average ion mass, a decrease in ion current, and a redistribution of voltage between the plasma and sheaths. These changes in turn cause a change in the power utilization efficiency. For dilute mixtures at silicon atomic flow ratios below 0.02, the useful power absorbed by electrons in the plasma is as much as 12% lower than mixtures that are more silicon rich. Thus, changes in power utilization can account for variations in growth rates of only 12% for different mixtures; the remaining, larger variations must be attributed to chemical or electron energy effects. Furthermore, changes in gas mixture do not cause large changes in silicon atomic flow ratio—for example, the substitution of Si_2H_6 or Si_3H_8 additives for comparable amounts of SiH_4—had no significant effect on power coupling or utilization efficiencies. Thus, the resulting effects of Si_2H_6 or Si_3H_8 additives on growth rates can be attributed purely to chemical or electron energy effects.

The determination and optimization of the power coupling and power utilization efficiencies made here will enable more conclusive evaluation of different gas additives and mixtures and more quantitative and detailed study of their chemistry. As an added benefit of this work, electrical signals were identified that can be used to detect a transient in the gas-phase density of silicon-containing molecules, faults or nonidealities in the rf power control circuitry, and changes in plasma radial uniformity. Such signals warrant further study and development, as they show promise for use in process monitoring and control.

[1]M. Matsumoto *et al.*, IEEE J. Photovoltaics **3**, 35 (2013).
[2]T. Matsui, H. Sai, K. Saito, and M. Kondo, Jpn. J. Appl. Phys., Part 1 **51**, 10NB04 (2012).
[3]T. Söderström, F.-J. Haug, V. Terrazzoni-Daudrix, and C. Ballif, J. Appl. Phys. **107**, 014507 (2010).
[4]J. K. Rath, Appl. Phys. A **96**, 145 (2009).
[5]M. N. van den Donker, T. Kilper, D. Grunsky, B. Rech, L. Houben, W. M. M. Kessels, and M. C. M. van de Sanden, Thin Solid Films **515**, 7455 (2007).
[6]M. N. van den Donker, B. Rech, W. M. M. Kessels, and M. C. M. van de Sanden, New J. Phys. **9**, 280 (2007).
[7]A. A. Howling, B. Strahm, P. Colsters, I. Sansonnens, and C. Hollenstein, Plasma Sour. Sci. Technol. **16**, 679 (2007).
[8]D. Mataras, Pure Appl. Chem. **77**, 379 (2005).
[9]M. A. Sobolewski, J. G. Langan, and B. S. Felker, J. Vac. Sci. Technol., B **16**, 173 (1998).
[10]K. L. Steffens and M. A. Sobolewski, IEEE Trans. Plasma Sci. **27**, 74 (1999).

Redistribution subject to AVS license or copyright; see http://scitation.aip.org/termsconditions. Download to IP: 129.6.144.75 On: Fri, 27 Jun 2014 17:35:22

[11]M. A. Sobolewski and K. L. Steffens, J. Vac. Sci. Technol., A **17**, 3281 (1999).
[12]Certain commercial instruments are identified to adequately specify the experimental procedure. In no case does such identification imply endorsement by N.I.S.T.
[13]M. A. Sobolewski, J. Vac. Sci. Technol., A **10**, 3550 (1992).
[14]J. W. Butterbaugh, L. D. Baston, and H. H. Sawin, J. Vac. Sci. Technol., A **8**, 916 (1990).
[15]M. A. Sobolewski, J. Appl. Phys. **100**, 063310 (2006).
[16]W. R. Entley, J. G. Langan, B. S. Felker, and M. A. Sobolewski, J. Appl. Phys. **86**, 4825 (1999).
[17]E. Amanatides, A. Hammad, E. Katsia, and D. Mataras, J. Appl. Phys. **97**, 073303 (2005).
[18]M. A. Lieberman, IEEE Trans. Plasma Sci. **17**, 338 (1989).
[19]M. A. Sobolewski, Appl. Phys. Lett. **70**, 1049 (1997).
[20]M. Long, IEEE Trans. Plasma Sci. **34**, 443 (2006).
[21]J. S. Yoon, M. Y. Song, J. M. Han, S. H. Hwang, W. S. Chang, and B. J. Lee, J. Phys. Chem. Ref. Data **37**, 913 (2008).
[22]K. Anzai *et al.*, Eur. Phys. J. D **66**, 36 (2012).
[23]H. Tanaka, L. Boesten, H. Sato, M. Kimura, M. A. Dillon, and D. Spence, J. Phys. B: At. Mol. Opt. Phys. **23**, 577 (1990).
[24]J.-S. Yoon, M.-Y. Song, H. Kato, M. Hoshino, H. Tanaka, M. J. Brunger, S. J. Buckman, and H. Cho, J. Phys. Chem. Ref. Data **39**, 033106 (2010).
[25]M. A. Dillon, L. Boesten, H. Tanaka, M. Kimura, and H. Sato, J. Phys. B: At. Mol. Opt. Phys. **27**, 1209 (1994).
[26]A. Zecca, G. P. Karwasz, and R. S. Brusa, Riv. Nuovo Cimento **19**, 1 (1996).
[27]J. F. Williams, J. Phys. B: At. Mol. Phys. **8**, 1683 (1975).
[28]M. Vinodkumar, C. Limbachiya, K. Korot, and K. N. Joshipura, Eur. Phys. J. D **48**, 333 (2008).
[29]E. Krishnakumar and S. K. Srivastava, Contrib. Plasma Phys. **35**, 395 (1995).
[30]R. Basner, M. Schmidt, V. Tarnovsky, K. Becker, and H. Deutsch, Int. J. Mass Spectrom. Ion Processes **171**, 83 (1997).
[31]V. Tarnovsky, H. Deutsch, and K. Becker, J. Chem. Phys. **105**, 6315 (1996).
[32]M. B. Shah, D. S. Elliott, and H. B. Gilbody, J. Phys. B: At. Mol. Phys. **20**, 3501 (1987).
[33]S. K. Srivastava, E. Krishnakumar, and A. C. d. A. e. Souza, Int. J. Mass Spectrom. Ion Processes **107**, 83 (1991).
[34]E. Krishnakumar and S. K. Srivastava, Int. J. Mass Spectrom. Ion Processes **103**, 107 (1991).
[35]E. Krishnakumar, S. Denifl, I. Cadez, S. Markelj, and N. J. Mason, Phys. Rev. Lett. **106**, 243201 (2011).
[36]L. A. Pinnaduwage and P. G. Datskos, J. Appl. Phys. **81**, 7715 (1997).
[37]M. Allan and S. F. Wong, Phys. Rev. Lett. **41**, 1791 (1978).
[38]J. Perrin, O. Leroy and M. C. Bordage, Contrib. Plasma Phys. **36**, 3 (1996).
[39]A. Gallagher, A. A. Howling, and C. Hollenstein, J. Appl. Phys. **91**, 5571 (2002).
[40]M. Shiratani, T. Fukuzawa, K. Eto, and Y. Watanabe, Jpn. J. Appl. Phys., Part 2 **31**, L1791 (1992).
[41]H. Nomura, A. Kono, and T. Goto, Jpn. J. Appl. Phys., Part 1 **35**, 3603 (1996).
[42]D. Nandi, S. A. Rangwala, S. V. K. Kumar, and E. Krishnakumar, Int. J. Mass Spectrom. **205**, 111 (2001).
[43]V. A. Godyak, R. B. Piejak, and B. M. Alexandrovich, IEEE Trans. Plasma Sci **19**, 660 (1991).
[44]L. J. Overzet and F. Y. Leong-Rousey, Plasma Sour. Sci. Technol. **4**, 432 (1995).
[45]A. J. Miranda and C. J. Spanos, J. Vac. Sci. Technol., A **14**, 1888 (1996).
[46]E. Amanatides and D. Mataras, J. Appl. Phys. **89**, 1556 (2001).
[47]G. Franz, J. Vac. Sci. Technol., A **23**, 369 (2005).
[48]K. Kohler, J. W. Coburn, D. E. Horne, E. Kay, and J. H. Keller, J. Appl. Phys. **57**, 59 (1985).
[49]H. Chatham and A. Gallagher, J. Appl. Phys. **58**, 159 (1985).
[50]E. A. G. Hamers, W. G. J. H. M. Van Sark, J. Bezemer, W. F. Van der Weg, and W. J. Goedheer, "Amorphous Silicon Technology - 1996," *14th Symposium on Amorphous Silicon Technology at the 1996 Materials Research Society (MRS) Spring Meeting*, San Francisco, CA, 8–12 April 1996 (Mater. Res. Soc. Symp. Proc., 1996), Vol. 420, pp. 461–466.
[51]D. O'Connell, R. Zorat, A. R. Ellingboe, and M. M. Turner, Phys. Plasmas **14**, 103510 (2007).
[52]M. A. Sobolewski and J.-H. Kim, J. Appl. Phys. **102**, 113302 (2007).
[53]D. Hrunski, W. Grählert, J. Beese, T. Kilper, A. Gordijn, and W. Appenzeller, Thin Solid Films **517**, 4188 (2009).
[54]S. Xu, X. Zhang, H. Ren, C. Wei, and Y. Zhao, Thin Solid Films **521**, 27 (2012).

Redistribution subject to AVS license or copyright; see http://scitation.aip.org/termsconditions. Download to IP: 129.6.144.75 On: Fri, 27 Jun 2014 17:35:22